




Micromechanical homogenization of a hydrogel-filled electrospun scaffold for tissue-engineered epicardial patching of the infarcted heart: a feasibility study

Kevin L. Sack · Nicolas Mandel · Nicola M. Pugno · Deon Bezuidenhout · Georges Limbert · Francesco Moscato · Neil H. Davies · Thomas Franz · Tamer Abdalrahman 

Received: 20 December 2021 / Accepted: 25 May 2023 / Published online: 1 July 2023
© The Author(s) 2023

Abstract For tissue engineering applications, accurate prediction of the effective mechanical properties of tissue scaffolds is critical. Open and closed cell modelling, mean-field homogenization theory, and finite element (FE) methods are theories and techniques currently used in conventional homogenization methods to estimate the equivalent mechanical properties of tissue-engineering scaffolds. This study aimed at developing a formulation to link the

microscopic structure and macroscopic mechanics of a fibrous electrospun scaffold filled with a hydrogel for use as an epicardial patch for local support of the infarcted heart. The macroscopic elastic modulus of the scaffold was predicted to be 0.287 MPa with the FE method and 0.290 MPa with the closed-cell model for the realistic fibre structure of the scaffold, and 0.108 MPa and 0.540 MPa with mean-field homogenization for randomly oriented and completely aligned fibres. The homogenized constitutive description of the scaffold was implemented for an epicardial

Kevin L. Sack, Nicolas Mandel These authors have equally contributed to this work.

K. L. Sack · N. Mandel · G. Limbert · T. Franz · T. Abdalrahman (✉)
Biomedical Engineering Research Centre, Division of Biomedical Engineering, Department of Human Biology, University of Cape Town, Cape Town, South Africa
e-mail: tamer.abdalrahman@uct.ac.za

K. L. Sack
Cardiac Rhythm Management, Medtronic Inc, Minneapolis, MN Minnesota, USA

N. Mandel · F. Moscato
University of Applied Sciences, Vienna, Austria

N. M. Pugno
Laboratory of Bio-Inspired & Graphene Nanomechanics, Department of Civil, Environmental and Mechanical Engineering, University of Trento, Trento, Italy

N. M. Pugno
School of Engineering and Materials Science, Queen Mary University, London, UK

N. M. Pugno
Ket-Lab, Edoardo Amaldi Foundation, Italian Space Agency, Rome, Italy

D. Bezuidenhout · N. H. Davies
Cardiovascular Research Unit, University of Cape Town, Cape Town, South Africa

G. Limbert · T. Franz
Bioengineering Science Research Group, Faculty of Engineering and Physical Sciences, University of Southampton, Southampton, UK

F. Moscato
Center for Medical Physics and Biomedical Engineering, Medical University of Vienna, Vienna, Austria

F. Moscato
Ludwig Boltzmann Institute for Cardiovascular Research, Vienna, Austria

F. Moscato
Austrian Cluster for Tissue Regeneration, Vienna, Austria

patch in a FE model of a human cardiac left ventricle to assess the effects of patching on myocardial mechanics and ventricular function in the presence of an infarct. Epicardial patching was predicted to reduce maximum myocardial stress in the infarcted LV from 19 kPa (no patch) to 9.5 kPa (patch) and to marginally improve the ventricular ejection fraction from 40% (no patch) to 43% (patch). This study demonstrates the feasibility of homogenization techniques to represent complex multiscale structural features in a simplified but meaningful and effective manner.

Keywords Fibrous scaffold · Myocardial infarction · Mean-field homogenization · Foam mechanics · Finite element method · Composite materials

1 Introduction

Cardiovascular disease (CVD) remains the leading cause of death worldwide. In 2013, roughly 30% of all deaths in the USA could be attributed to cardiovascular disease [1]. Myocardial infarction (MI), one of the most significant contributors to CVD, is caused by a blockage of the blood supply to the myocardium that initiates ischemia and subsequent tissue death [2–4]. Increasing distention of the left ventricle induces cellular processes that lead to stronger degeneration. Post-infarct treatment concepts aim at halting degenerative progress. Intramyocardial biomaterial injection and epicardial patching are two promising approaches to counteract the deleterious effects of ventricular distention by favourably altering the underlying mechanics of the heart [5, 6]. Epicardial patches are designed to mechanically support the infarct area of the myocardium following a MI, reducing myocardial wall stress and preventing left ventricular dilatation and remodelling as a result. Previous studies have reported the therapeutic effects of various patches on MI [7–16] and the advantages of structural support from these patches to the myocardial wall [9, 11, 13]. However, the optimum patch design has not yet been found due to a limited understanding of mechanisms restricting left ventricular remodelling and restoring cardiac function.

Both patching and injection therapy can benefit impaired myocardium in two ways. The first is the delivery of bioactive compounds into the

myocardium. These compounds influence the pathobiological pathways mobilized by MI and intervene either through paracrine signalling or through the delivery of active growth factors [5, 6, 17, 18]. The second is the mechanical support that biomaterial injectates and epicardial patches can provide to the impaired myocardium [5, 18, 19], which has been shown to decrease adverse remodelling [8].

Patching treatment concepts have grown significantly due to improved cell retention capabilities, relative ease in delivering bioactive molecules, substantial mechanical support [18], and easy tailoring to specific sizes and shapes. Patches are almost exclusively made up of porous scaffold structures consisting of interconnecting fibrous networks or foam-type materials. Scaffold characteristics depend on the manufacturing method of fabrication (e.g., electrospinning, 3D printing [20]), the underlying material choice (e.g., polymer, decellularised matrices [21]), and the length scales of the structure (i.e., fibre diameter and pore size). The variety of these methods leads to a wide range of structural properties of scaffolds on both the macro- and micro-scale.

The combination of electrospun fibrous scaffolds and hydrogels has been previously studied [22–27] and is a promising treatment concept, exploiting the advantages that each material offers. Different structures and mechanical properties from both groups of materials combined with different fabrication techniques can lead to a large variety of compound materials [28].

The extracellular microenvironment transmits two types of cues, i.e. biochemical and biophysical. Biochemical cues mainly refer to signalling from neighbouring cells, growth factors, extracellular matrix (ECM) proteins, and oxygen levels [29]. Although the effects of biochemical signals in cardiac regeneration have been extensively investigated [30–32], one aspect of the biophysical signals still needs more study [33]. It is generally accepted that the mechanical regulation of ECM plays a key role in maintaining tissue homeostasis, such as cell proliferation, differentiation, and function [34–36]. In order to achieve ideal treatments, we need to understand the cell behaviour as a function of its microenvironment. Hence, as in the current study, one main interest lies in understanding the mechanical deformation of engineered cellular environments, such as an electrospun polymeric scaffold filled with a hydrogel.

The mechanical characterization of these combined materials is scarcely described. Different theories have been used to obtain the homogenized mechanical properties, e.g. micromechanical homogenization [37–40] and the closed-cell model [41–43]. For composite materials with well-dispersed reinforcements, the impact of the reinforcements can be assessed with a mean-field approach. This approach involves resembling the surrounding area of each reinforcement as the matrix [44] (Mori–Tanaka method) or as the composite [45] (Self-Consistent). Kundanati et al. [46] obtained the elastic modulus of a silk scaffold filled with silk hydrogel matrix in compression tests and compared the results to analytical data from a combination of open-cell and closed-cell models [47][43, 48, 49]. Their results showed an increase in the elastic modulus of the composite compared to either of the primary structural components, and experimental and analytical results were similar. Strange et al. [50] determined the elastic modulus of a polycaprolactone electrospun scaffold filled with alginate hydrogels of different concentrations in the indentation and tensile tests. They report strain toughening behaviour similar to conventional composite materials but found substantial differences between the two test methods.

The current study aimed to link the microscopic and macroscopic mechanical descriptions of a hydrogel-filled electrospun polymeric scaffold and to explore the use of such a scaffold as an epicardial patch for treating MI. Analytical and numerical models were combined to (i) develop a homogenized macroscopic description of the mechanics of the scaffold and (ii) identify the effects of the scaffold stiffness as an epicardial patch on left-ventricular mechanics and function in the infarcted heart.

2 Materials and methods

This study is divided into two parts: (I) Determination of the homogenized elastic modulus of an electrospun hydrogel-filled scaffold using a finite element (FE) model and comparison to analytical models. (II) Investigation of treating an acute left ventricular (LV) infarct with an epicardial

electrospun hydrogel-filled scaffold patch. The absence of voids inside the hydrogel was assumed.

2.1 Homogenization of hydrogel-filled scaffold

Pellethane© 2363–80AE (Lubrizol, Ohio, USA), a medical-grade aromatic poly (ether urethane) with a hard segment consisting of 4,4-methylenebis(phenylisocyanate) and 1,4-butanediol and a soft segment of poly (tetramethylene oxide) glycol ($M_n = 1000$ g/mole) [51] were used.

A 15 wt% Pellethane© solution was obtained by dissolving 8 g of Pellethane© pellets in 53.3 g of tetrahydrofuran (THF, source) at 37 °C for 8 h. The Pellethane© solution was electrospun from a hypodermic needle (SE400B syringe pump, Fresenius, Bad Homburg, Germany) onto a rotating and bidirectionally translating tubular target (hypodermic tubing, Small Parts, Logansport, IN, USA) using a custom-made rig. The spinning process parameters were: solution flow rate 6 mL/h, target outer diameter 25.0 mm, target rotating speed 4400 rpm, target translational speed 2.6 mm/min, potential difference 13 kV, and source-target distance 250 mm.

2.1.1 Geometrical reconstruction

Micro-computed tomography (μ CT) images of the electrospun fibrous scaffold obtained at the University of Southampton were processed with the Simpleware ScanIP (Synopsys, Mountain View, CA, USA), see Fig. 1a. The spatial parameters of the μ CT images are provided in Table 1. A central region of the scaffold sample was selected to provide a representative volume element (RVE) of the scaffold's interconnected fibre structure. Fibre surfaces were smoothed, and any residual islands of fibres were excluded. The mean fibre diameter was 6.7 μ m. The reconstructed geometry of the scaffold RVE is presented in Fig. 1b. To simulate the complete filling of the fibrous scaffold with hydrogel, void space between the fibres of the scaffold RVE was identified in Simpleware by inverting the scaffold mask and treated as a hydrogel domain, as illustrated in Fig. 1c. The fibrous scaffold was assumed to be filled entirely without leaving any voids.

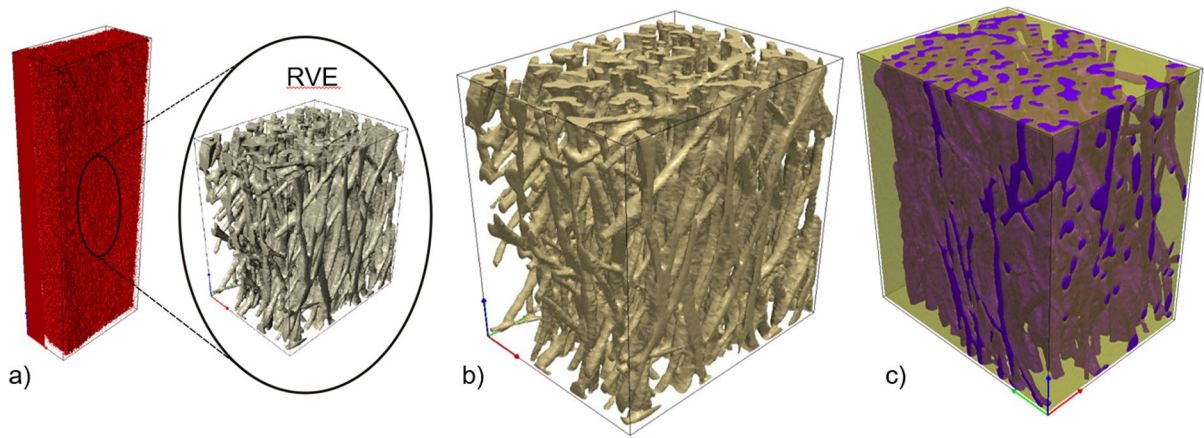


Fig. 1 (a) μ CT representation of electrospun scaffold sample and the smaller central representative volume element (RVE). (b) 3D reconstructed geometry of the representative volume

Table 1 Basic spatial properties of scaffold μ CT data for the RVE

Axis	Image extent (mm)	Spacing (mm)	Voxel extent
X	0.2226	0.0021	106
Y	0.2877	0.0021	137
Z	0.3213	0.0021	153

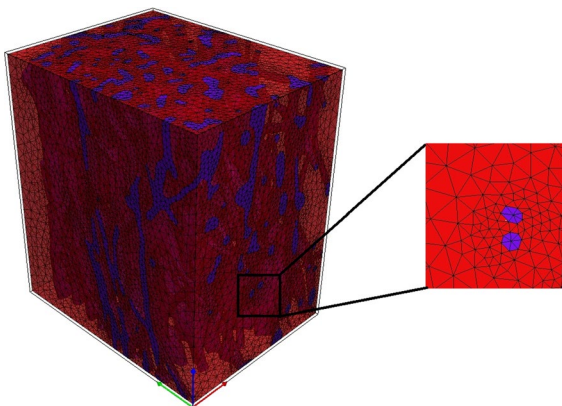


Fig. 2 Fibrous scaffold and hydrogel mesh with a close-up to illustrate the mesh refinement in the vicinity of fibre-hydrogel interfaces

2.1.2 Finite element modelling

2.1.2.1 Mesh generation The scaffold and hydrogel geometries were meshed using tetrahedral ele-

ment of the electrospun scaffold. (c) Electrospun scaffold (purple) filled with hydrogel (beige, opacity = 70%)

ments (Simpleware). Continuous transitions were implemented between scaffold fibres and hydrogel, with mesh refinement near fibre-hydrogel interfaces, see Fig. 2. The RVE comprised scaffold fibres with a volume fraction of 21.6% and 364,429 elements and hydrogel with a volume fraction of 78.4% and 524,580 elements. The meshed geometry was imported into Abaqus Standard (Dassault Systèmes, Simulia, Corp., Johnston, RI, USA).

2.1.2.2 Constitutive laws The static equilibrium equation is used to calculate the deformation of an elastic body [52]:

$$\text{div } \boldsymbol{\sigma}(\boldsymbol{\epsilon}(\mathbf{u})) + \mathbf{f} = 0 \tag{1}$$

where \mathbf{f} is external forces and \mathbf{u} are displacements, and the strain tensor [52] can be linearized as

$$\boldsymbol{\epsilon}(\mathbf{u}) = \frac{1}{2}(\nabla \mathbf{u}^T + \nabla \mathbf{u})$$

$$\mathbf{u} = \begin{cases} u = 0 & z = 0 \\ u_x = u_y = 0 & z = l \\ u_z = 0.1 * l & z = l \end{cases} \tag{2}$$

where l is the length of the RVE in the z -direction.

The scaffold fibres and hydrogel were represented with a neo-Hookean strain energy density function ψ [51, 53, 54] defined as:

$$\psi = \frac{\mu}{2}(I_1 - 3) + \frac{k}{2}(J - 1)^2 \tag{3}$$

where μ and k are the ground state shear and bulk modulus, respectively. I_1 and J are the first and third invariants of the right Cauchy-Green deformation tensor, \mathbf{B} . The latter is given by:

$$\mathbf{B} = \mathbf{F}^T \mathbf{F} \tag{4}$$

where \mathbf{F} is the deformation gradient tensor [52]. The values of the neo-Hookean material parameters used for the scaffold fibres and the hydrogel are provided in Table 2.

2.1.2.3 Boundary conditions and loading The boundary conditions of the RVE used are shown in Fig. 3. One RVE surface was fixed in all directions, and a displacement was applied normally to the opposite surface. The degrees of freedom of the nodes of the remaining surfaces were left unconstrained. These boundary conditions generated a uniform tensile strain field up to $\epsilon = 0.1$ (equivalent to a stretch $\lambda = 1.1$).

2.1.3 Homogenization techniques

2.1.3.1 Computational model Uniaxial stretch corresponding to a maximum of 10% global (i.e. macroscopic) strain was simulated with the FE model of the hydrogel-filled scaffold. Volume-averaged nominal strain $\langle \epsilon \rangle$ and nominal stress $\langle \sigma \rangle$ in loading direction were obtained by volume normalization to account for variable element sizes and meshing anomalies and used to calculate the homogenized elasticity, \mathbf{E} , according to

$$\langle \sigma \rangle = E \langle \epsilon \rangle \tag{5}$$

2.1.3.2 Analytical model of homogenization (a) MEAN-FIELD HOMOGENIZATION

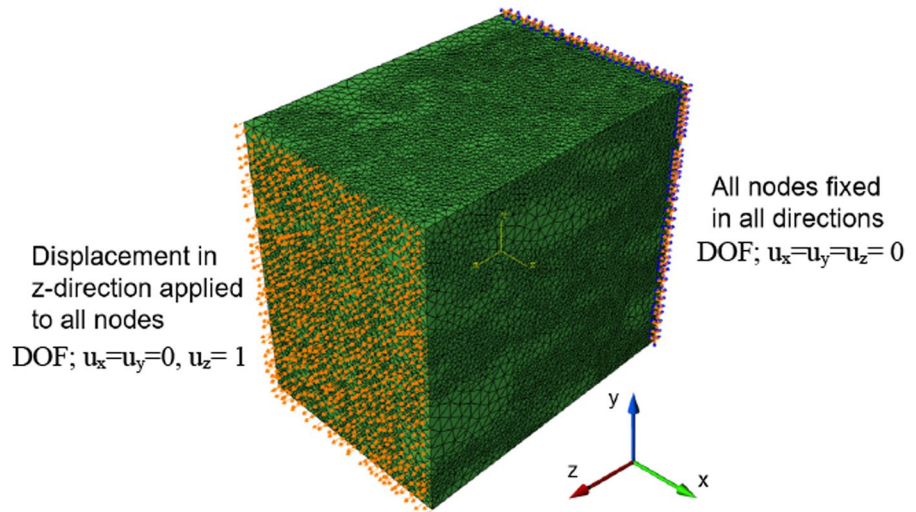
Mean-field (MF) homogenization of the mechanical properties of the scaffold-hydrogel composite was undertaken by analysis of the RVE described above. The RVE served as a statistical representation of material properties, as shown in Fig. 1. It is generally postulated that the RVE contains enough information to describe the behaviour of a microstructure [57].

The mean-field homogenization theories used for the scaffold are based on the principle that the

Table 2 Mechanical properties of scaffold material and hydrogel

Component	Constitutive law	Parameters
Scaffold fibres	Neo-Hookean elasticity	$\mu = 0.96$ MPa, $k = 2.08$ MPa [55]
Hydrogel	Neo-Hookean elasticity	$\mu = 0.35$ kPa, $k = 3.33$ kPa [56]

Fig. 3 Illustration of boundary conditions, degrees of freedom (DOF), and loading of the scaffold RVE model



fibre length (l) is very large compared to the fibre radius (R) so that the aspect ratio l/R equals infinity ($l/R = \infty$).

In the case of a two-phase composite, the strain field over an RVE comprising the inclusion phase and matrix phase are related by the following relationships:

$$\langle \epsilon \rangle = f_i \langle \epsilon \rangle_i + f_m \langle \epsilon \rangle_m \quad (6)$$

$$\epsilon_i = \mathbf{A} \epsilon_m \quad (7)$$

where f is the volume fraction and the subscripts i and m refer to the inclusion phase and the matrix phase, respectively. The average strain for each phase is correlated by a strain concentration tensor \mathbf{A} . It can be found from Eshelby's solution [58] that strain inside an inclusion (ϵ) is uniform and related to the remote strain (Ω):

$$\epsilon(x) = \mathbf{H}(l, \mathbf{C}_m, \mathbf{C}_i) : \Omega \quad (8)$$

where \mathbf{C}_i and \mathbf{C}_m are the stiffnesses of the inclusion and matrix respectively, $:$ is the matrix scalar product, and \mathbf{H} is the strain concentration tensor of a single inclusion defined as:

$$\mathbf{H}(l, \mathbf{C}_m, \mathbf{C}_i) = \{ \mathbf{I} + \xi : \mathbf{C}_m^{-1} : [\mathbf{C}_i - \mathbf{C}_m] \}^{-1} \quad (9)$$

where ξ is the Eshelby tensor [58].

According to the Mori–Tanaka homogenization approach, the strain concentration tensor \mathbf{A} and the strain concentration tensor \mathbf{H} of the single inclusion problem are assumed to be equal [58, 59]. Additionally, Mori–Tanaka's model considers each inclusion as a separate inclusion in a matrix subjected to the

average matrix strain (ϵ_m) as a far-field [44]. The effective stiffness can be given by

$$\mathbf{C}^{eff} = \mathbf{C}_m + f_i (\mathbf{C}_i - \mathbf{C}_m) \mathbf{H}^{MT} \quad (10)$$

where \mathbf{H}^{MT} is the Mori–Tanaka strain concentration tensor [60].

Two cases were assumed for the MF analytical model, namely that (1) the fibres are fully aligned along a unique main direction, and (2) the fibres are randomly oriented.

(b) FOAM MECHANICS

The mechanical behaviour of the fibrous scaffold can be predicted by using the open cell model where the elastic modulus of the fibrous scaffold is obtained by [47]:

$$\frac{E_s^*}{E_s} = \left(\frac{\rho^*}{\rho_s} \right)^2 \quad (11)$$

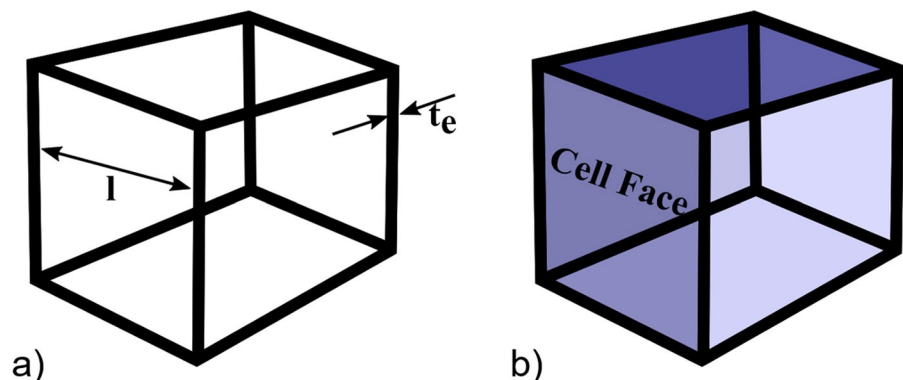
where E_s , ρ_s , E^* , and ρ^* are elastic moduli and density of the individual fibres and the fibrous scaffold, respectively.

The homogenized elastic modulus of the scaffold filled with hydrogel can be estimated by assuming the cell is filled with hydrogel, as shown in Fig. 4. The homogenized elastic modulus E_{hom} can be calculated using a formula provided by Gibson and Ashby [47]:

$$E_{hom} \approx \left\{ \varphi^2 \left(\frac{\rho^*}{\rho_s} \right)^2 E_s + (1 - \varphi) \left(\frac{\rho^*}{\rho_s} \right) E_s \right\} + E_m \quad (12)$$

where φ is the ratio of the volume of the edge to the total volume of the face and E_m is the elastic modulus of the hydrogel matrix. The contributions of edge

Fig. 4 Illustration of (a) an open-cell model was used to estimate the elastic modulus of the fibrous scaffold without hydrogel and (b) a closed-cell model with edges and faces was used to predict the elastic modulus of the fibrous scaffold with hydrogel



bending and face stretching are represented by the first and the second term, respectively, and the contribution of the hydrogel matrix is represented by the third term.

The homogenization process is based on deformations of the approximated unit cell. In the model of Kundanati et. al [46], the solid fraction of the cell edges can be estimated with

$$\Phi = \frac{t_e^2}{t_e^2 + \frac{n_f}{n_e} t_f l} \tag{13}$$

This relationship describes the solid fraction amount contained in the compression-bearing edges and faces as the primary determinant for mechanical stability, with n_f and n_e as the number of faces meeting at an edge and the number of edges of a face, respectively, and l as the size of a single pore [61]. For approximation, the face thickness t_f and edge thickness t_e were considered equal and of the value of the fibre diameter of 6.7 μm .

2.2 The cardiac left ventricle and epicardial patch

2.2.1 Geometrical reconstruction

The geometry of a left ventricle was reconstructed, using the segmentation capabilities of Simpleware ScanIP, for a normal human subject utilizing the data from Genet et al. [62]. An acute infarct in the LV free wall was simulated in the anterior wall, mid-way between the base and apex of the heart. Infarction was assumed to affect tissue within a radius of 25 mm, resulting in a fully transmural infarct. The outer ring of the infarct, i.e., 15–25 mm from the centre of the infarct, was assumed to transition linearly from fully infarcted to healthy tissue based on radial distance. This transition avoids sharp discontinuities in tissue properties and is physiologically more representative. For the treated infarct case with an epicardial patch, a layer with a thickness of 0.2 mm [63] was added to the epicardial ventricular surface in the infarct region (Fig. 5). The effect of patch stiffness on left ventricular stress distribution and cardiac pressure–volume loop was investigated. The patch stiffness was obtained by homogenization theory based on the fibre orientation.

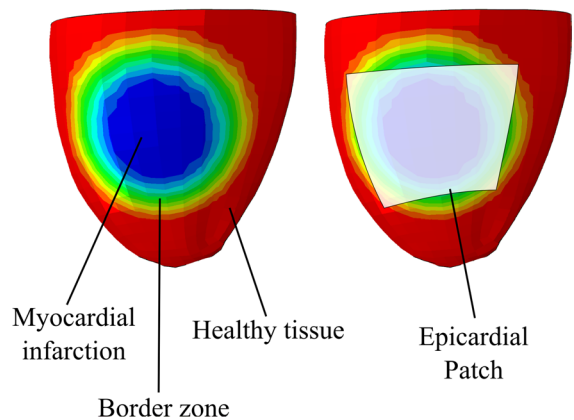


Fig. 5 Schematic illustration of an LV showing the description of myocardial infarction (MI) and the patch placement. Red regions are fully healthy myocardium, blue regions are fully infarcted myocardium, and the colours between illustrating the linear transition from healthy to infarcted tissue

2.2.2 Finite element modelling

Cardiac simulations used the same LV geometry for the healthy case, untreated acute MI case, and acute MI case with an epicardial patch. Pressure–volume curves and myocardial stresses were captured and used to assess the treatment effects of the epicardial patch.

2.2.2.1 Mesh generation LV geometry was meshed into approximately 3,500 linear hexahedral elements using Simpleware ScanIP. A hybrid constant pressure–linear displacement formulation was selected in Abaqus (C3D8H element code). The homogenized patch was meshed using 72 quadrilateral shell elements (S4R element code, arranged in a 9×8 grid, using the underlying hexahedral element faces). The resulting patch dimensions ranged from 33–50 mm in the circumferential direction and 40 mm in the longitudinal direction. These dimensions were chosen to cover the infarcted tissue while not overly encroaching on the healthy tissue. As the patch and LV geometry share global nodes of the FE mesh, the degrees of freedom of the patch were coupled to those of the myocardial surface. This constraint aligns with a patch attached epicardially using surgical adhesive.

2.2.2.2 Constitutive laws The passive mechanics of cardiac tissue were represented using a continuum fibre-reinforced composite approach following

Holzappel and Ogden [64]. The isochoric and volumetric responses are governed by the strain energy potentials:

$$\Psi_{iso} = \frac{a}{2b} e^{b(I_1-3)} + \sum_{i=f,s} \frac{a_i}{2b_i} \left\{ e^{b_i(I_i-1)^2} - 1 \right\} + \frac{a_{fs}}{2b_{fs}} \left\{ e^{b_{fs}(I_{8fs})^2} - 1 \right\}, \quad (14)$$

$$\Psi_{vol} = \frac{1}{D} \left(\frac{J^2 - 1}{2} - \ln(J) \right) \quad (15)$$

Equation (14) is defined through eight material parameters a , b , a_f , b_f , a_s , b_s , a_{fs} , b_{fs} , and four strain invariants that deal with isotropic deformation, I_1 , deformation in the fibre and sheet direction, I_{4f} and I_{4s} respectively, and shear deformation that couples the fibre-sheet plane, I_{8fs} .

Equation (15) is defined through J and a penalty term D , which is inversely proportional to the bulk modulus ($D=2/K=0.1 \text{ MPa}^{-1}$) and therefore characterizes the degree of compressibility. For a deformation that is perfectly volume-preserving, $J=1$.

This constitutive material model for passive myocardial mechanics (Eqs. 14 and 15) ensures that the material exhibits the well-documented exponential and anisotropic strain response to strain [65–67] while enforcing near incompressibility.

The description of the time-varying elastance model of active force [68] development is specified as:

$$T_a(t, l) = T_{MAX} \frac{Ca_0^2}{Ca_0^2 + ECa_{50}^2(l)} \frac{(1 - \cos(\omega(t, l)))}{2} \quad (16)$$

where T_{max} , the maximum allowable active tension, is multiplied by a term governing the calcium concentration and a term governing the contraction timing. Both terms depend on sarcomere length l , which depends on the strain in the fibre direction. The active tension generated from this representation captures length-dependent effects such as Frank Starling's Law [69].

For the finite element analyses, the infarcted left ventricle was represented by altering material parameters of the myocardium in the infarct region such that the myocardium was non-contractile and half as stiff as the healthy tissue, representative of

Table 3 Constitutive parameters for the passive and active material response of healthy and infarcted myocardium

Material parameters	Healthy	Infarcted
a (kPa)	0.276	0.138
b (-)	6.09	6.09
a_f (kPa)	0.908	0.454
b_f (-)	11.69	11.69
a_s (kPa)	0.126	0.063
b_s (-)	10.14	10.14
a_{fs} (kPa)	0.074	0.037
b_{fs} (-)	2.50	2.50
T_{max}	130	0.0

an acute ischemic MI [70]. A functional border zone (see Fig. 5) was implemented by linearly transitioning the elastic modulus and contractility from the infarct region to the healthy tissue region. The key material parameters for healthy and infarcted myocardium are provided in Table 3.

2.2.2.3 Homogenized patch A linear elastic model based on Hooke's law was used to describe the mechanical properties of the patch, with the value for the elastic modulus obtained from homogenization techniques and the assumption of near incompressibility (Poisson's ratio $\nu=0.45$).

2.2.2.4 Boundary conditions and loading In the LV model, all nodes on the truncated base were fixed in-plane. The endocardial ring of the LV truncated base was coupled to a fictitious fixed point at its centre using a distributed kinematic constraint to prevent rigid body translation.

The FE model of the LV was coupled to a lumped circulatory model to simulate pressure loading consistent with the physiological beating heart [71]. As only a single illustrative cardiac cycle of the left ventricle was modelled, the pulmonary circuit and returning venous flow were disengaged from the systemic circuit, effectively only engaging the systemic circuit during LV ejection. This was sufficient to simulate one cardiac cycle. The circulatory model parameters taken from Sack et al. [71] were fixed across simulations, ensuring the different cases experienced the same pre- and after-load during the cardiac cycle. During diastole, the LV endocardial surface experiences gradual loading until a

pressure of 12 mmHg is reached. During systole, the cavity pressure depends on the force generation of the contracting LV interacting with the lumped circulatory model.

3 Results

3.1 Scaffold homogenization

The strain and stress distributions in the scaffold predicted by the FE model exhibit significant heterogeneity, with concentrations of strain and stress up to four orders of magnitude higher than the average

values (Fig. 6a and b). The hydrogel displays strain one order of magnitude higher than those in the scaffold fibres (Fig. 6c), whereas the stress in the hydrogel (Fig. 6b) is one order of magnitude smaller than that in the scaffold fibres (Fig. 6d).

The homogenized elastic modulus of the RVE based on nominal stress and nominal strain in the loading direction obtained from the FE simulation ($E_{\text{hom}}=0.287$ MPa) was very similar to that predicted with the closed-cell model derivation ($E_{\text{hom}}=0.29$ MPa), see Fig. 7. The mean-field homogenization for completely aligned and randomly oriented fibres predicted a higher ($E_{\text{hom}}=0.540$ MPa) and lower modulus

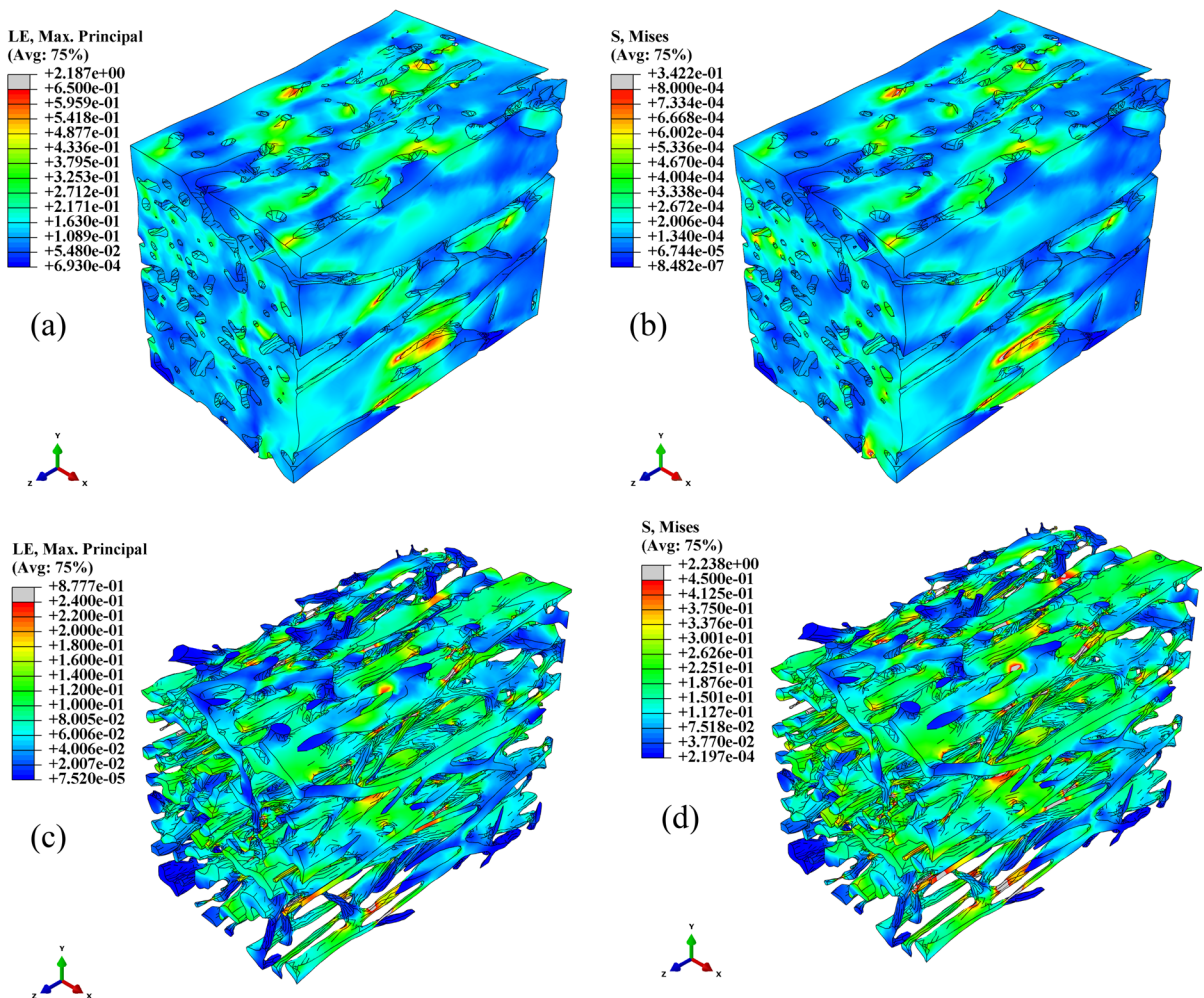


Fig. 6 Contour plots of the logarithmic maximum principal strain (a) and von Mises stress (MPa) (b) in the hydrogel and of the logarithmic maximum principal strain (c) and von Mises stress (MPa) (d) in the scaffold structure

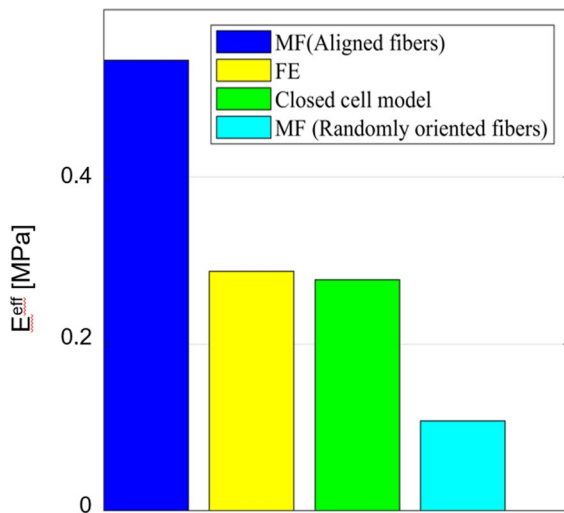


Fig. 7 Effective elastic moduli of the scaffold-hydrogel RVE were obtained with different methods of homogenization (Mean Field (MF), Finite Element (FE))

($E_{hom} = 0.108$ MPa) than the FE and closed cell results.

3.2 Treatment effect of epicardial patching

The results of the LV in the healthy state, with untreated MI, and with MI treated with an epicardial patch show a slight improvement of stroke volume with an epicardial patch compared to the untreated case, albeit lower than the healthy condition (Fig. 8a).

The patch provides mechanical restraint (i.e., limiting the infarct-related dilation at the end of passive filling) and elastic support (i.e., the stretched patch, stored with elastic energy at the end of passive filling, assisting the contractile function of the heart). These effects collectively resulted in an improved cardiac ejection fraction of 43% for patch treatment with an elastic modulus of 0.287 MPa compared to an ejection fraction of 40% for the untreated infarct.

The patch also affected the distribution and magnitude of the myocardial stress. High stresses in the untreated infarct were not observed in the infarcted LV with patch treatment (Fig. 8b). The maximum value for myocardial stress decreased

from $1.9e^{-2}$ MPa in the untreated infarct to $0.95e^{-2}$ MPa for the infarct with the patch with an elastic modulus of 0.287 MPa.

4 Discussion

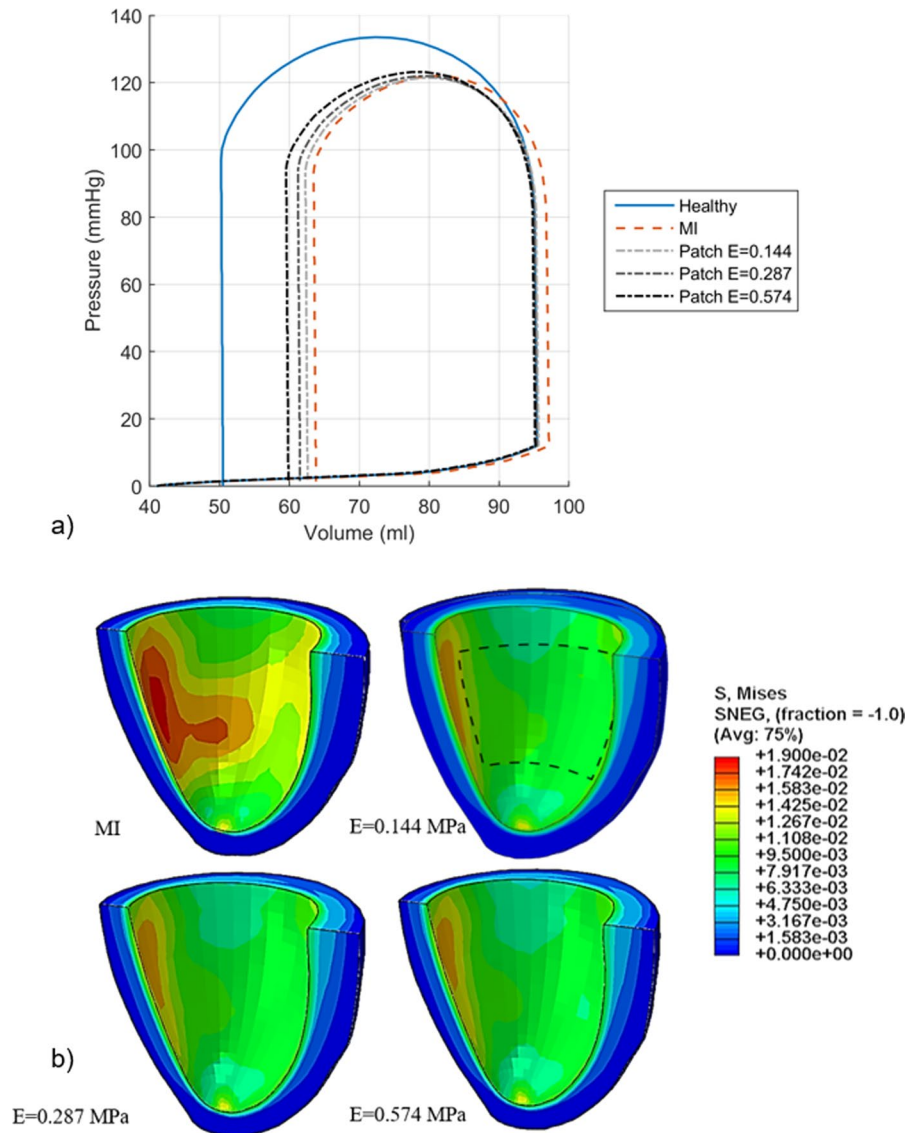
Fibrous scaffolds have received attention for their use as cardiovascular tissue engineering patches [72]. However, limitations of patches include poor control of cell differentiation and unmatched mechanical properties [73]. Advancing the understanding of how the epicardial patch improves cardiac performance will enable translation toward clinical application.

In this study, we investigated (i) the micro- and macro-mechanics of an electrospun polymeric scaffold filled with a hydrogel and (ii) the effect of such a scaffold as an epicardial patch on myocardial mechanics and ventricular function in the presence of a myocardial infarct. A comparison of three homogenization methodologies, including open-cell modeling, homogenization theory, and the finite element method, was provided to predict the effective properties of heterogeneous and porous tissue scaffolds.

A scaffold model was constructed from μ CT images of fibrous electrospun material. The hydrogel was assumed to fill the void space between the fibres. Material properties for bulk polyurethane elastomer and a gentrified hydrogel were used [55, 56]. The model is based on simplified concepts of macro- and microscopic features of the scaffold, hydrogel, and cardiac loading. In the current simulation, the ventricular loading was simplified to maximal distention as specified in the literature [74].

In general, the scaffold's global elasticity is a function of the scaffold materials and the overall porosity of the scaffold structure. The effective elasticity of the scaffold decreases from fully aligned to random fibre orientation (Fig. 7). The findings suggest that fibre orientations may be a critical component when assessing the overall structural properties of the electrospun fibrous scaffold. A hydrogel-filled scaffold will result in different mechanical stress distributions at the microstructure level than a scaffold without hydrogel. This may majorly impact the cells that interact with the scaffold at the microscopic level. A global elastic modulus of the hydrogel-filled scaffold of 0.287 MPa was obtained from FE homogenization. This value is

Fig. 8 The application of an idealized patch to treat myocardial infarction improves function and regional stress within the heart. **(a)** Pressure volume loops comparing the cardiac output of the LV in a healthy state, with MI and with MI and patch treatment. **(b)** The stress (MPa) distribution shown over half the LV reveals the endocardial surface of the “patched” region of the heart. The patch position is outlined in black dashed lines



set between the upper (0.540 MPa) and lower limit (0.108 MPa) of the elastic modulus for completely aligned and randomly oriented fibres predicted by mean-field homogenization. Considering that the electrospun scaffold exhibited partially aligned fibres (Fig. 1a), and the close agreement with the result of the closed-cell model verifies the image-based finite element homogenization method and results.

The differences between the upper and lower bound of the elastic modulus and the FE and open-cell prediction are based on the effect of the fibre orientation in the representative volume element. These effects of the microstructure morphology

(including porosity, pore shape, and pore size) may be optimized by topology optimization techniques [75] combined with the 3D printing technique. A major technological achievement of 3D printing is the capacity to build a physical framework of biocompatible materials for clinical application and control their mechanical properties. Fibre alignment and organization of scaffolds for epicardial patches should be easily adjustable [76] at the manufacturing phase to provide optimized mechanical properties in line with the complex mechanical nature of the cardiac activity. The simulation of the LV with MI demonstrated that applying the epicardial patch, with

material parameters derived through homogenization, resulted in moderately improved stroke volume. The patch also reduced the peak wall stress in the acutely infarcted region. Decreased wall stress can provide a long-term benefit for the recovery and inhibition of adverse heart remodelling following MI [77, 78]. The model presented here can be modified and updated towards a design guide for epicardial patches to a dynamic viscoelastic characteristic of the hydrogel, resulting in an adaptable, dynamic stiffness that regulates the patch's properties in response to the periodic deformation of the ventricular wall.

While the range of elastic moduli presented here is representative of the hydrogel-filled scaffold investigated in this study, a more comprehensive investigation using the techniques presented here would be of more value. The microstructural properties of the myocardial patch (e.g. scaffold stiffness, porosity, fibre alignment) may be optimized along with the macrostructural properties (e.g. patch shape, thickness, orientation, anisotropy) using a combined analytical and *in silico* approach to developing a myocardial patch with optimal therapeutic benefits. Furthermore, future work could address the application of myocardial patches to more detailed patient-specific FE models to understand the implications of personalizing the therapy to individuals. A more comprehensive analysis of patch stiffness and optimization of the stiffness difference between the therapeutic patch and infarcted myocardium (exploring sensitivity to infarct size, border zone, stiffness, and their evolution over time) will be useful.

The FE homogenization method provides a basis to guide epicardial patching in computational mechanical cardiac models of MI to optimize therapeutic effects. The approach can provide a computational framework for systematically screening structural and material combinations of hydrogels and electrospun fibres. The same framework may be used complementarily in multi-objective design optimization studies. In that context, a numerical optimizer would seek the structural and mechanical properties of individual material phases of the composite patch that lead to its optimal mechanical properties/performance for a given patient-specific treatment.

The developed model demonstrates the value of homogenization techniques to represent complex multiscale features in a simplified yet meaningful and effective manner. The current study provided insight

into the mechanical benefits of a patch for a potential MI therapy. The approach proposed here is primarily a proof-of-concept methodology. Further validation and sensitivity analyses must be conducted before this model can realistically provide clinical insight.

5 Conclusion

The current work is a first step toward developing and exploiting an *in silico* platform to mechanistically predict the links between the material and structural properties of the individual constituents of a tissue-engineering scaffold and its macroscopic or homogenized mechanical properties. Such a prediction will enable truly bridging length scales from cells to tissues and organs to optimize treatment plan strategies and procedures for epicardial patching for specific patients and outcomes. The analytical method and computational models developed for the micromechanical homogenization of a composite scaffold offer potential for application to other tissue engineering and regenerative medicine areas. Such scaffolds can offer tailored mechanical support and biological benefits through controlled and targeted drug release. Future work will focus on extending the computational framework to cellular and sub-cellular length scales to account for cellular mechanics.

Acknowledgements The research reported in this publication was supported by the National Research Foundation of South Africa (UID 92531 and 93542), and the South African Medical Research Council under a Self-Initiated Research Grant (SIR 328148). Views and opinions expressed are not those of the NRF or MRC but of the authors. Nicola M. Pugno was supported by the European Commission with the Graphene Flagship Core 2 No 785219 (WP14 “Composites”) and FET Proactive “Neurofibres” No. 732344 as well as by the Italian Ministry of Education, University and Research with the “Departments of Excellence” grant L. 232/2016 and ARS01-01384-PROSCAN.

Funding Open access funding provided by University of Cape Town.

Data availability Abaqus models of the scaffold and the left ventricle used in this study are available on ZivaHub at <http://doi.org/10.25375/uct.12894872>

Declarations

Conflicts of interest The authors declare that they have no conflict of interest.

Open Access This article is licensed under a Creative Commons Attribution 4.0 International License, which permits use, sharing, adaptation, distribution and reproduction in any medium or format, as long as you give appropriate credit to the original author(s) and the source, provide a link to the Creative Commons licence, and indicate if changes were made. The images or other third party material in this article are included in the article's Creative Commons licence, unless indicated otherwise in a credit line to the material. If material is not included in the article's Creative Commons licence and your intended use is not permitted by statutory regulation or exceeds the permitted use, you will need to obtain permission directly from the copyright holder. To view a copy of this licence, visit <http://creativecommons.org/licenses/by/4.0/>.

References

- Mozaffarian D, Benjamin EJ, Go AS et al (2016) Heart disease and stroke statistics-2016 update a report from the American heart association. *Circulation* 133:e38–e48. <https://doi.org/10.1161/CIR.0000000000000350>
- Saleh M, Ambrose JA (2018) Understanding myocardial infarction [version 1; referees: 2 approved]. *Research*. <https://doi.org/10.12688/f1000research.15096.1>
- Kalogeris T, Baines CP, Krenz M, Korthuis RJ (2012) Cell biology of ischemia/reperfusion injury. *Int Rev Cell Mol Biol* 298:229–317. <https://doi.org/10.1016/B978-0-12-394309-5.00006-7>
- Chiong M, Wang ZV, Pedrozo Z et al (2011) Cardiomyocyte death: mechanisms and translational implications. *Cell Death Dis* 2:e244–e244. <https://doi.org/10.1038/cddis.2011.130>
- Hinderer S, Brauchle E, Schenke-Layland K (2015) Generation and assessment of functional biomaterial scaffolds for applications in cardiovascular tissue engineering and regenerative medicine. *Adv Healthc Mater* 4:2326–2341. <https://doi.org/10.1002/adhm.201400762>
- Wang H, Rodell CB, Zhang X et al (2018) Effects of hydrogel injection on borderzone contractility post-myocardial infarction. *Biomech Model Mechanobiol* 17:1533–1542. <https://doi.org/10.1007/s10237-018-1039-2>
- Liao SY, Siu CW, Liu Y et al (2010) Attenuation of left ventricular adverse remodeling with epicardial patching after myocardial infarction. *J Card Fail* 16:590–598. <https://doi.org/10.1016/j.cardfail.2010.02.007>
- D'Amore A, Yoshizumi T, Luketich SK et al (2016) Bilayered polyurethane—Extracellular matrix cardiac patch improves ischemic ventricular wall remodeling in a rat model. *Biomaterials* 107:1–14. <https://doi.org/10.1016/j.biomaterials.2016.07.039>
- Fomovsky GM, Clark SA, Parker KM et al (2012) Anisotropic reinforcement of acute anteroapical infarcts improves pump function. *Circ Hear Fail* 5:515–522. <https://doi.org/10.1161/CIRCHEARTFAILURE.111.965731>
- Chi NH, Yang MC, Chung TW et al (2013) Cardiac repair using chitosan-hyaluronan/silk fibroin patches in a rat heart model with myocardial infarction. *Carbohydr Polym* 92:591–597. <https://doi.org/10.1016/j.carbpol.2012.09.012>
- Enomoto Y, Gorman JH, Moainie SL et al (2005) Early ventricular restraint after myocardial infarction: extent of the wrap determines the outcome of remodeling. *Ann Thorac Surg* 79:881–887. <https://doi.org/10.1016/j.athoracsur.2004.05.072>
- Serpooshan V, Zhao M, Metzler SA et al (2013) The effect of bioengineered acellular collagen patch on cardiac remodeling and ventricular function post myocardial infarction. *Biomaterials* 34:9048–9055. <https://doi.org/10.1016/j.biomaterials.2013.08.017>
- Moainie SL, Guy TS, Gorman JH et al (2002) Infarct restraint attenuates remodeling and reduces chronic ischemic mitral regurgitation after postero-lateral infarction. *Ann Thorac Surg* 74:444–449. [https://doi.org/10.1016/S0003-4975\(02\)03747-5](https://doi.org/10.1016/S0003-4975(02)03747-5)
- Stuckey DJ, Ishii H, Chen QZ et al (2010) Magnetic resonance imaging evaluation of remodeling by cardiac elastomeric tissue scaffold biomaterials in a rat model of myocardial infarction. *Tissue Eng Part A* 16:3395–3402. <https://doi.org/10.1089/ten.tea.2010.0213>
- Vilaeti AD, Dimos K, Lampri ES et al (2013) Short-term ventricular restraint attenuates post-infarction remodeling in rats. *Int J Cardiol* 165:278–284. <https://doi.org/10.1016/j.ijcard.2011.08.036>
- Fujimoto KL, Tobita K, Guan J et al (2012) Placement of an elastic biodegradable cardiac patch on a subacute infarcted heart leads to cellularization with early developmental cardiomyocyte characteristics. *J Card Fail* 18:585–595. <https://doi.org/10.1016/j.cardfail.2012.05.006>
- Zhu Y, Matsumura Y, Wagner WR (2017) Ventricular wall biomaterial injection therapy after myocardial infarction: advances in material design, mechanistic insight and early clinical experiences. *Biomaterials* 129:37–53
- Günter J, Wolint P, Bopp A, et al (2016) Microtissues in cardiovascular medicine: regenerative potential based on a 3D microenvironment. *Stem Cells Int* 2016
- Emmert MY, Hitchcock RW, Hoerstrup SP (2014) Cell therapy, 3D culture systems and tissue engineering for cardiac regeneration. *Adv Drug Deliv Rev* 69–70:254–269
- Gao L, Kupfer ME, Jung JP et al (2017) Myocardial tissue engineering with cells derived from human-induced pluripotent stem cells and a native-like, high-resolution, 3-dimensionally printed scaffold. *Circ Res* 120:1318–1325. <https://doi.org/10.1161/CIRCRESAHA.116.310277>
- Wan L, Chen Y, Wang Z et al (2017) Human heart valve-derived scaffold improves cardiac repair in a murine model of myocardial infarction. *Sci Rep*. <https://doi.org/10.1038/srep39988>
- Strange DGT, Tonsomboon K, Oyen ML (2012) Electrospun fiber—Hydrogel composites for nucleus pulposus tissue engineering. In: *materials Research Society Symposium Proceedings*. pp 35–40
- Agrawal A, Rahbar N, Calvert PD (2013) Strong fiber-reinforced hydrogel. *Acta Biomater* 9:5313–5318. <https://doi.org/10.1016/j.actbio.2012.10.011>
- Castellano D, Blanes M, Marco B et al (2014) A comparison of electrospun polymers reveals poly(3-hydroxybutyrate) fiber as a superior scaffold for cardiac repair. *Stem*

- Cells Dev 23:1479–1490. <https://doi.org/10.1089/scd.2013.0578>
25. Moutos FT, Freed LE, Guilak F (2007) A biomimetic three-dimensional woven composite scaffold for functional tissue engineering of cartilage. *Nat Mater* 6:162–167. <https://doi.org/10.1038/nmat1822>
 26. Castilho M, Hochleitner G, Wilson W et al (2018) Mechanical behavior of a soft hydrogel reinforced with three-dimensional printed microfibre scaffolds. *Sci Rep*. <https://doi.org/10.1038/s41598-018-19502-y>
 27. Brunelle AR, Horner CB, Low K et al (2018) Electrospun thermosensitive hydrogel scaffold for enhanced chondrogenesis of human mesenchymal stem cells. *Acta Biomater* 66:166–176. <https://doi.org/10.1016/j.actbio.2017.11.020>
 28. Bosworth LA, Turner LA, Cartmell SH (2013) State of the art composites comprising electrospun fibres coupled with hydrogels: a review. *Nanomedicine Nanotechnology. Biol Med* 9:322–335
 29. Schaller MD (2001) Biochemical signals and biological responses elicited by the focal adhesion kinase. *Biochim Biophys Acta Mol Cell Res* 1540:1–21. [https://doi.org/10.1016/S0167-4889\(01\)00123-9](https://doi.org/10.1016/S0167-4889(01)00123-9)
 30. Liu YW, Fang YH, Su CT et al (2019) The biochemical and electrophysiological profiles of amniotic fluid-derived stem cells following Wnt signaling modulation cardiac differentiation. *Cell Death Discov* 5:1–11. <https://doi.org/10.1038/s41420-019-0143-0>
 31. Broughton KM, Wang BJ, Firouzi F et al (2018) Mechanisms of cardiac repair and regeneration. *Circ Res* 122:1151–1163. <https://doi.org/10.1161/CIRCRESAHA.117.312586>
 32. Santini MP, Winn N, Rosenthal N (2006) Signalling pathways in cardiac regeneration. *Novartis Found Symp* 274:228–238. <https://doi.org/10.1002/0470029331.ch14>
 33. Lin CD, Falanga M, De Lauro E et al (2021) Biochemical and biophysical mechanisms underlying the heart and the brain dialog. *AIMS Biophys* 8:1–33. <https://doi.org/10.3934/biophys.2021001>
 34. Gupta V, Grande-Allen KJ (2006) Effects of static and cyclic loading in regulating extracellular matrix synthesis by cardiovascular cells. *Cardiovasc Res* 72:375–383. <https://doi.org/10.1016/j.cardiores.2006.08.017>
 35. Lu P, Takai K, Weaver VM, Werb Z (2011) Extracellular Matrix degradation and remodeling in development and disease. *Cold Spring Harb Perspect Biol*. <https://doi.org/10.1101/cshperspect.a005058>
 36. Urbanczyk M, Layland SL, Schenke-Layland K (2020) The role of extracellular matrix in biomechanics and its impact on bioengineering of cells and 3D tissues. *Matrix Biol* 85–86:1–14. <https://doi.org/10.1016/j.matbio.2019.11.005>
 37. Gangwar T, Heuschele DJ, Annor G et al (2021) Multiscale characterization and micromechanical modeling of crop stem materials. *Biomech Model Mechanobiol* 20:69–91. <https://doi.org/10.1007/s10237-020-01369-6>
 38. Bianchi D, Morin C, Badel P (2020) Implementing a micromechanical model into a finite element code to simulate the mechanical and microstructural response of arteries. *Biomech Model Mechanobiol* 19:2553–2566. <https://doi.org/10.1007/s10237-020-01355-y>
 39. Muhlestein MB, Haberman MR (2016) A micromechanical approach for homogenization of elastic metamaterials with dynamic microstructure. *Proc R Soc A Math Phys Eng Sci*. <https://doi.org/10.1098/rspa.2016.0438>
 40. Ryu S, Lee S, Jung J et al (2019) Micromechanics-based homogenization of the effective physical properties of composites with an anisotropic matrix and interfacial imperfections. *Front Mater* 6:1–17. <https://doi.org/10.3389/fmats.2019.00021>
 41. Fahlbusch NC, Becker W (2011) Effective mechanical properties of closed-cell foams investigated with a microstructural model and numerical homogenisation. *Adv Struct Mater* 15:549–560. https://doi.org/10.1007/978-3-642-21855-2_36
 42. Luo G, Zhu Y, Zhang R et al (2021) A review on mechanical models for cellular media: Investigation on material characterization and numerical simulation. *Polymers (Basel)*. <https://doi.org/10.3390/polym13193283>
 43. Gan YX, Chen C, Shen YP (2005) Three-dimensional modeling of the mechanical property of linearly elastic open cell foams. *Int J Solids Struct* 42:6628–6642. <https://doi.org/10.1016/j.ijsolstr.2005.03.002>
 44. Benveniste Y (1987) A new approach to the application of Mori-Tanaka's theory in composite materials. *Mech Mater* 6:147–157. [https://doi.org/10.1016/0167-6636\(87\)90005-6](https://doi.org/10.1016/0167-6636(87)90005-6)
 45. Hill R (1965) A self-consistent mechanics of composite materials. *J Mech Phys Solids* 13:213–222. [https://doi.org/10.1016/0022-5096\(65\)90010-4](https://doi.org/10.1016/0022-5096(65)90010-4)
 46. Kundanati L, Singh SK, Mandal BB et al (2016) Fabrication and mechanical characterization of hydrogel infused network silk scaffolds. *Int J Mol Sci*. <https://doi.org/10.3390/ijms17101631>
 47. Gibson LJ, Ashby MF (2014) Cellular solids: structure and properties, second edition, 2nd editio. Cambridge University Press
 48. Luo G, Zhu Y, Zhang R et al (2021) A review on mechanical models for cellular media: investigation on material characterization and numerical simulation. *Polymers (Basel)* 13:3283. <https://doi.org/10.3390/polym13193283>
 49. Ashby MF (1983) Mechanical properties of cellular solids. *Metall Trans A Phys Metall Mater Sci* 14A:1755–1769. <https://doi.org/10.1007/BF02645546>
 50. Strange DGT, Tonsomboon K, Oyen ML (2014) Mechanical behaviour of electrospun fibre-reinforced hydrogels. *J Mater Sci Mater Med* 25:681–690. <https://doi.org/10.1007/s10856-013-5123-y>
 51. Baaijens FPT, Trickey WR, Laursen TA, Guilak F (2005) Large deformation finite element analysis of micropipette aspiration to determine the mechanical properties of the chondrocyte. *Ann Biomed Eng* 33:494–501. <https://doi.org/10.1007/s10439-005-2506-3>
 52. Nair S (2012) Introduction to continuum mechanics. In: introduction to continuum mechanics. pp xiii–xiv
 53. Breuls RGM, Sengers BG, Oomens CWJ et al (2002) Predicting local cell deformations in engineered tissue constructs: a multilevel finite element approach. *J Biomech Eng* 124:198–207. <https://doi.org/10.1115/1.1449492>
 54. Peeters EAG, Oomens CWJ, Bouten CVC et al (2005) Mechanical and failure properties of single attached cells under compression. *J Biomech* 38:1685–1693. <https://doi.org/10.1016/j.jbiomech.2004.07.018>
 55. Cambridge University Engineering Department (2003) Materials data book: 2003 Edition

56. Bachmann B, Spitz S, Schädl B et al (2020) Stiffness matters: fine-tuned hydrogel elasticity alters chondrogenic redifferentiation. *Front Bioeng Biotechnol* 8:1–12. <https://doi.org/10.3389/fbioe.2020.00373>
57. Czyż T, Dziatkiewicz G, Fedeliński P et al (2013) Advanced computer modelling in micromechanics. Silesian University of Technology Press, Gliwice
58. Eshelby JD (1957) The determination of the elastic field of an ellipsoidal inclusion, and related problems. *Proc R Soc London Ser A Math Phys Sci* 241:376–396. <https://doi.org/10.1098/rspa.1957.0133>
59. Pierard O, Friebel C, Doghri I (2004) Mean-field homogenization of multi-phase thermo-elastic composites: a general framework and its validation. *Compos Sci Technol* 64:1587–1603. <https://doi.org/10.1016/j.compscitech.2003.11.009>
60. Fritsch A, Hellmich C (2007) “Universal” microstructural patterns in cortical and trabecular, extracellular and extravascular bone materials: micromechanics-based prediction of anisotropic elasticity. *J Theor Biol* 244:597–620. <https://doi.org/10.1016/j.jtbi.2006.09.013>
61. Krynauw H (2016) Tailoring of the biomechanics of tissue-regenerative vascular scaffolds. University of Cape Town
62. Genet M, Lee LC, Nguyen R et al (2014) Distribution of normal human left ventricular myofiber stress at end diastole and end systole: a target for in silico design of heart failure treatments. *J Appl Physiol* 117:142–152. <https://doi.org/10.1152/jappphysiol.00255.2014>
63. Lin X, Liu Y, Bai A et al (2019) A viscoelastic adhesive epicardial patch for treating myocardial infarction. *Nat Biomed Eng* 3:632–643. <https://doi.org/10.1038/s41551-019-0380-9>
64. Holzapfel GA, Ogden RW (2009) Constitutive modelling of passive myocardium: a structurally based framework for material characterization. *Philos Trans R Soc A Math Phys Eng Sci* 367:3445–3475. <https://doi.org/10.1098/rsta.2009.0091>
65. Demer LL, Yin FC (1983) Passive biaxial mechanical properties of isolated canine myocardium. *J Physiol* 339:615–630. <https://doi.org/10.1113/jphysiol.1983.sp014738>
66. Hunter PJ, McCulloch AD, Ter Keurs HEDJ (1998) Modelling the mechanical properties of cardiac muscle. *Prog Biophys Mol Biol* 69:289–331. [https://doi.org/10.1016/S0079-6107\(98\)00013-3](https://doi.org/10.1016/S0079-6107(98)00013-3)
67. Dokos S, Smaill BH, Young AA, LeGrice IJ (2002) Shear properties of passive ventricular myocardium. *Am J Physiol Hear Circ Physiol*. <https://doi.org/10.1152/ajpheart.00111.2002>
68. Guccione JM, McCulloch AD (1993) Mechanics of active contraction in cardiac muscle: Part I—constitutive relations for fiber stress that describe deactivation. *J Biomech Eng* 115:72–81. <https://doi.org/10.1115/1.2895473>
69. Solaro RJ (2007) Mechanisms of the Frank-Starling law of the heart: the beat goes on. *Biophys J* 93:4095–4096. <https://doi.org/10.1529/biophysj.107.117200>
70. Holmes JW, Borg TK, Covell JW (2005) Structure and mechanics of healing myocardial infarcts. *Annu Rev Biomed Eng* 7:223–253. <https://doi.org/10.1146/annurev.bioeng.7.060804.100453>
71. Sack KL, Aliotta E, Ennis DB et al (2018) Construction and validation of subject-specific biventricular finite-element models of healthy and failing swine hearts from high-resolution DT-MRI. *Front Physiol*. <https://doi.org/10.3389/fphys.2018.00539>
72. Carrier RL, Papadaki M, Rupnick M et al (1999) Cardiac tissue engineering: cell seeding, cultivation parameters, and tissue construct characterization. *Biotechnol Bioeng* 64:580–589. [https://doi.org/10.1002/\(SICI\)1097-0290\(19990905\)64:5%3c580::AID-BIT8%3e3.0.CO;2-X](https://doi.org/10.1002/(SICI)1097-0290(19990905)64:5%3c580::AID-BIT8%3e3.0.CO;2-X)
73. Robinson KA, Li J, Mathison M et al (2005) Extracellular matrix scaffold for cardiac repair. *Circulation*. <https://doi.org/10.1161/CIRCULATIONAHA.104.525436>
74. Jeung MY, Germain P, Croisille P et al (2012) Myocardial tagging with MR imaging: overview of normal and pathologic findings. *Radiographics* 32:1381–1398. <https://doi.org/10.1148/rg.325115098>
75. Gogarty E, Pasini D (2015) Hierarchical topology optimization for bone tissue scaffold: preliminary results on the design of a fracture fixation plate. *Comput Methods Appl Sci* 38:311–340. https://doi.org/10.1007/978-3-319-18320-6_17
76. Grasl C, Stoiber M, Röhrich M et al (2021) Electrospinning of small diameter vascular grafts with preferential fiber directions and comparison of their mechanical behavior with native rat aortas. *Mater Sci Eng C*. <https://doi.org/10.1016/j.msec.2021.112085>
77. Grossman W, Jones D, McLaurin LP (1975) Wall stress and patterns of hypertrophy in the human left ventricle. *J Clin Invest* 56:56–64. <https://doi.org/10.1172/JCI108079>
78. Yin FC (1981) Ventricular wall stress. *Circ Res* 49:829–842

Publisher’s Note Springer Nature remains neutral with regard to jurisdictional claims in published maps and institutional affiliations.